Journal of Magnetic Resonance 203 (2010) 91–99

Contents lists available at ScienceDirect

Journal of Magnetic Resonance

journal homepage: www.elsevier.com/locate/jmr

Designing gradient coils with reduced hot spot temperatures

Peter T. While [a,*], Larry K. Forbes [a], Stuart Crozier [b]

[a] School of Mathematics & Physics, University of Tasmania, Private Bag 37, Hobart, Tasmania 7001, Australia
[b] School of Information Technology & Electrical Engineering, University of Queensland, St. Lucia, Brisbane, Qld 4072, Australia

ARTICLE INFO

Article history:
Received 25 August 2009
Revised 17 November 2009
Available online 24 December 2009

Keywords:
Magnetic resonance imaging (MRI)
Gradient coil design
Temperature
Heating
Cooling
Thermal
Hot spot
Inverse method
Optimisation
Non-linear

ABSTRACT

Gradient coil temperature is an important concern in the design and construction of MRI scanners. Closely spaced gradient coil windings cause temperature hot spots within the system as a result of Ohmic heating associated with large current being driven through resistive material, and can strongly affect the performance of the coils. In this paper, a model is presented for predicting the spatial temperature distribution of a gradient coil, including the location and extent of temperature hot spots. Subsequently, a method is described for designing gradient coils with improved temperature distributions and reduced hot spot temperatures. Maximum temperature represents a non-linear constraint and a relaxed fixed point iteration routine is proposed to adjust coil windings iteratively to minimise this coil feature. Several examples are considered that assume different thermal material properties and cooling mechanisms for the gradient system. Coil winding solutions are obtained for all cases considered that display a considerable drop in hot spot temperature ($> 20\%$) when compared to standard minimum power gradient coils with equivalent gradient homogeneity, efficiency and inductance. The method is semi-analytical in nature and can be adapted easily to consider other non-linear constraints in the design of gradient coils or similar systems.

1. Introduction

The design of gradient coils is an inverse optimisation problem in which either coil current magnitudes, coil winding positions or current density modes are obtained subject to some desired magnetic field being induced within the imaging volume. One well established design method is that of Turner [1], in which a Fourier–Bessel expansion is used to describe the magnetic field and Fourier Transforms are used to find the appropriate current density solution. The over-determined nature of the problem demands that an additional feature of the coil be minimised along with the target field error, following a Lagrange multiplier argument, and common choices include inductance [2] and power [3]. The current density solution may be related to a streamfunction and contours taken to yield discrete coil windings (see also, [4]).

Fourier Transforms have the undesirable feature of operating on an infinite spatial domain and hence the target field method demands apodising functions to yield sensible coil windings. Carlson et al. [5] instead propose a Fourier series representation of the current density to address the finite nature of the coil, and coil length is constrained explicitly using a Turner-style target field method by Chronik and Rutt [6]. Forbes and Crozier [7] obtain a finite length coil without approximation by combining a Fourier series expansion with Tikhonov regularisation to solve an ill-conditioned integral equation (see for example, [8, p. 307]). A further extension to this method is given by While et al. [9] who explore the extra degree of freedom available to the current density in 3D solution space.

High image resolution demands strong field gradients and hence high coil currents. However, due to the resistive properties of the coil material this results in local Joule heating, which is a considerable concern in the operation of gradient coils and can lead to image distortion or damage to the coils. Typically, cooling pipes carrying water are included in the gradient system to ensure coil temperature remains below an acceptable level (see for example, [10–12]).

Average coil temperature is modelled as a function of time by Chu and Rutt [13], who compare predictions to the experimental results of five coils. Their model includes Ohmic heating, radial conductive, convective and radiative cooling, and predicts a steady-state temperature reached via an inverse exponential function of time. The model of Chu and Rutt [13] is extended in the present paper by considering the important transfer mechanisms of axial and azimuthal conduction of heat through the copper layer of the coil. The steady-state solution allows local temperature variations to be predicted, rather than simply the average temperature of the entire coil, apparently for the first time. Many material properties of the coil can be varied and different cooling mechanisms can be considered such as convective air, forced air and forced water cooling. A common feature of the temperature distributions

* Corresponding author. Fax: +61 3 62262410.
E-mail address: pwhile@utas.edu.au (P.T. While).

1090-7807/$ - see front matter Crown Copyright © 2009 Published by Elsevier Inc. All rights reserved.
doi:10.1016/j.jmr.2009.12.004

is the existence of hot spots that occur in regions of high current density, or equivalently, in regions where the coil windings are closely spaced (see also, [13]). It is these hot spots that are then targeted in the coil design method proposed subsequently in the present paper.

Very few design methods in the literature consider the temperature of gradient coils in their optimisation routines. The spacing of coil windings is targeted directly in the design method of Poole et al. [14] who manually manipulate matrix elements relating to a streamfunction differential between adjacent node points in a boundary element mesh. The result is a redistribution of coil windings allowing higher efficiency coils for a given wire spacing at the expense of an increase in coil inductance. Leggett et al. [15] develop an average temperature model for a multi-layer gradient design. Those authors weight a power constraint in their optimisation routine according to layer position and this alters the distribution of windings between layers to enhance cooling.

In the present paper, an optimisation strategy for the current density is proposed with the aim of obtaining gradient coils with lower hot spot temperatures. This is a highly non-linear problem as it involves a maximum temperature constraint (l_∞-norm) rather than a quadratic constraint like power, inductance or overall temperature (l_2-norm). A functional involving the square of the gradient of the temperature is calculated and this is minimised using a relaxed fixed point iteration routine. The resultant current density solutions show a considerable drop in maximum temperature when compared to minimum power solutions with equivalent coil performance parameters.

The following section firstly presents an overview of the spatial temperature distribution model. In addition, Section 2 contains a detailed description of the optimisation strategy used for minimising the gradient hot spot temperature. In Section 3, temperature distributions for a minimum power x-gradient coil are compared with results from implementing the maximum temperature minimisation routine, for a variety of cases. Finally, some concluding remarks and a discussion of possible future work are given in Section 4.

2. Minimising hot spot temperature

In this section, a method will be introduced for designing gradient coil winding patterns with reduced maximum temperatures. Firstly, the spatial temperature distribution model will be presented, along with the means for obtaining a minimum power x-gradient coil. This solution will then be used in an iterative optimisation routine for minimising the gradient coil hot spot temperature.

2.1. Temperature distribution model

The geometry of the problem is displayed in Fig. 1 and involves a copper sheet of radius r_c, length $2L$ and thickness w, embedded in an insulating coil former of the same length, extending outwards to a radius of r_o and inwards to a radius of r_i. Chu and Rutt [13] provide a temporal heat equation for the average temperature of this type of arrangement, which includes Ohmic heating of the copper layer as a result of current within resistive material, radial conduction through the insulating former, and radial convective and radiative heat loss to the environment outside the coil system. Here we extend this heat equation to include the spatial qualities of axial and azimuthal dissipation of heat via conduction through the copper layer, and a spatial surface current density vector $\mathbf{j}(\theta', z')$ rather than some fixed current value. The resultant heat equation for the temperature difference between the copper layer and the environment, $T^* = T - T_{env}$ (K), as a function of position and time, is therefore chosen to be:

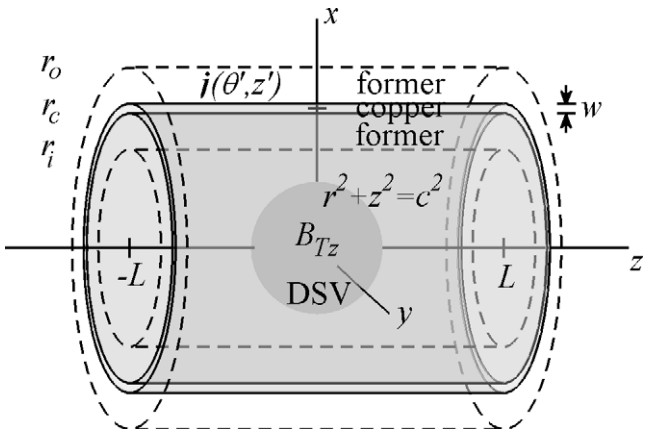

Fig. 1. The model used to describe a gradient coil comprising of a thin cylindrical copper sheet embedded in an insulating former. The copper sheet carries a surface current density $\mathbf{j}(\theta', z')$ and has length $2L$, radius r_c and thickness w. The insulating former has length $2L$ and extends radially outwards from the copper layer to a radius r_o and inwards to a radius r_i.

$$\rho_d c_h \frac{\partial T^*}{\partial t} = k_c \nabla^2 T^* + \frac{\rho_r}{w^2}\mathbf{j}\cdot\mathbf{j} - \frac{h_t}{w}T^*. \tag{1}$$

Eq. (1) involves the following material properties of copper: density $\rho_d = 8960\ \mathrm{kg/m^3}$, specific heat $c_h = 385\ \mathrm{J/kg/K}$, thermal conductivity $k_c = 401\ \mathrm{W/m/K}$, and resistivity $\rho_r = 1.68\times10^{-8}\ \Omega\mathrm{m}$. The term on the left-hand side of Eq. (1) represents the rate of change of internal energy within the coil. The first term on the right-hand side represents the conductive transfer of heat over the copper layer and is governed by Fourier's law (see for example, [16, p. 6] and [17, p. 121]). The second term on the right-hand side of Eq. (1) represents the Ohmic heating by current density $\mathbf{j}$ (A/m). Finally, the last term is a Newton's cooling term (see for example, [16, p. 12] and [17, p. 19]) representing the radial heat loss conductively through the former and convectively and radiatively to the environment. This cooling term involves a total heat transfer coefficient, h_t, given by [13]:

$$h_t = \left[\frac{\Delta r_i}{k_f} + \frac{r_c}{r_i h_i}\right]^{-1} + \left[\frac{\Delta r_o}{k_f} + \frac{r_c}{r_o h_o}\right]^{-1} + h_r\left(\epsilon_i\frac{r_i}{r_c} + \epsilon_o\frac{r_o}{r_c}\right). \tag{2}$$

Eq. (2) contains the distances $\Delta r_i = r_c - r_i$ and $\Delta r_o = r_o - r_c$. The thermal conductivity of the epoxy resin former is chosen to be $k_f = 0.6\ \mathrm{W/m/K}$ (see for example, [13,15]). The emissivities of the inner and outer surfaces are chosen to be $\epsilon_i = \epsilon_o = 0.9$ and the radiative heat transfer coefficient is set approximately with the value $h_r = 7.8\ \mathrm{W/m^2/K}$ (see [13]). Lastly, the convective heat transfer coefficients of the inner and outer surfaces are given the approximate values of $h_i = h_o = 10\ \mathrm{W/m^2/K}$ for convective air cooling, $h_i = h_o = 100\ \mathrm{W/m^2/K}$ for forced air cooling and $h_i = h_o = 1000\ \mathrm{W/m^2/K}$ for forced water cooling (see for example, [13]).

Primary interest lies with the spatial temperature distribution such that the location and extent of hot spots can be predicted. Therefore the steady-state form of Eq (1) is considered by setting the right-hand side to zero, and this is rewritten as follows:

$$\left[\nabla^2_{2D} - \frac{h_t}{k_c w}\right]T^*_{ss} = \frac{-\rho_r}{k_c w^2}\mathbf{j}\cdot\mathbf{j}. \tag{3}$$

Note that an approximate time-dependent solution to Eq. (1), giving the hot spot temperature as a function of time, can be obtained by linearising the first term on the right-hand side of Eq. (1) and considering the maximum current density. This results in an inverse exponential function of time, similar to the model of Chu and Rutt [13] for the average coil temperature, and can be used to check that the steady-state solution to Eq. (3) is reached within the time frame of a typical scanning scenario.

Eq. (3) is a 2D screened Poisson equation and can be solved using Green's functions; however, it is computationally faster and more convenient to consider a Fourier series solution to Eq. (3). In addition, a Fourier series form enables simple calculation of such functions as ∇T^*, which will be used in the optimisation routine presented later in this section. The linear nature of Eq. (3) for the steady-state temperature T^*_{ss} (relative to the environment) allows a general solution to be obtained involving a superposition of a particular integral type solution, T^*_{ssPI}, to Eq. (3) and a complementary function type solution, T^*_{ssCF}, to the homogeneous form of Eq. (3). That is, the general solution to Eq. (3) is chosen to be of the form:

$$T^*_{ssFS}(\theta,z) = T^*_{ssPI}(\theta,z) + T^*_{ssCF}(\theta,z). \tag{4}$$

where

$$\begin{aligned} T^*_{ssPI}(\theta,z) = F_{00} &+ \sum_{n=1}^{N_T}\left[C_{0n}\sin\left(\frac{n\pi(z+L)}{2L}\right) + F_{0n}\cos\left(\frac{n\pi(z+L)}{2L}\right)\right] \\ &+ \sum_{m=1}^{M_T}[F_{m0}\cos m\theta + G_{m0}\sin m\theta] \\ &+ \sum_{m=1}^{M_T}\sum_{n=1}^{N_T}\left\{\sin\left(\frac{n\pi(z+L)}{2L}\right)[C_{mn}\cos m\theta + D_{mn}\sin m\theta]\right. \\ &\left.+ \cos\left(\frac{n\pi(z+L)}{2L}\right)[F_{mn}\cos m\theta + G_{mn}\sin m\theta]\right\}. \end{aligned} \tag{5}$$

and

$$\begin{aligned} T^*_{ssCF}(\theta,z) = J_0\exp\left(\sqrt{\frac{h_t}{k_c w}}z\right) &+ P_0\exp\left(-\sqrt{\frac{h_t}{k_c w}}z\right) \\ &+ \sum_{u=1}^{U}\left\{[J_u\cos u\theta + K_u\sin u\theta]\exp\left(\sqrt{\left(\frac{u}{a}\right)^2+\frac{h_t}{k_c w}}z\right)\right. \\ &\left.+ [P_u\cos u\theta + Q_u\sin u\theta]\exp\left(-\sqrt{\left(\frac{u}{a}\right)^2+\frac{h_t}{k_c w}}z\right)\right\}. \end{aligned} \tag{6}$$

The expression for T^*_{ssPI} (5) contains the coefficients $C_{0n}, F_{0n}, F_{m0}, G_{m0}, C_{mn}, D_{mn}, F_{mn}$ and $G_{mn} (m = 1 : M_T, n = 1 : N_T)$, which can be obtained by substituting Eq. (5) into Eq. (3). For example, we obtain:

$$\begin{aligned} C_{mn} = \frac{1}{2\pi L}&\left[\left(\frac{m}{a}\right)^2 + \left(\frac{n\pi}{2L}\right)^2 + \frac{h_t}{k_c w}\right]^{-1}\frac{\rho_r}{k_c w^2} \\ &\times \int_{-L}^{3L}\int_{-\pi}^{\pi}\mathbf{j}(\theta',z')\cdot\mathbf{j}(\theta',z')\cos m\theta'\sin\left(\frac{n\pi(z'+L)}{2L}\right)d\theta' dz'. \end{aligned} \tag{7}$$

The expression for T^*_{ssCF} (6) contains the coefficients J_0, P_0, J_u, K_u, P_u and $Q_u (u = 1 : U)$, which are subject to boundary conditions on $z = \pm L$. These boundary conditions are chosen such as to provide an accurate match to the Green's function solution of Eq. (3), and result in coefficients of the form:

$$\begin{aligned} P_u = -\frac{1}{e}&\left[\exp\left(2\sqrt{\left(\frac{u}{a}\right)^2+\frac{h_t}{k_c w}}L\right) - \exp\left(-2\sqrt{\left(\frac{u}{a}\right)^2+\frac{h_t}{k_c w}}L\right)\right]^{-1} \\ &\times\left\{F_{u0}\left[\exp\left(\sqrt{\left(\frac{u}{a}\right)^2+\frac{h_t}{k_c w}}L\right) - \exp\left(-\sqrt{\left(\frac{u}{a}\right)^2+\frac{h_t}{k_c w}}L\right)\right]\right. \\ &\left.+\sum_{n=1}^{N_T}F_{un}\left[\exp\left(\sqrt{\left(\frac{u}{a}\right)^2+\frac{h_t}{k_c w}}L\right) - (-1)^n\exp\left(-\sqrt{\left(\frac{u}{a}\right)^2+\frac{h_t}{k_c w}}L\right)\right]\right\}. \end{aligned} \tag{8}$$

Expressions for the remaining coefficients are similar but not shown in interests of space.

2.2. Minimum power gradient coil

A method will be presented shortly for redesigning gradient coils such that hot spot temperatures are reduced. However, this non-linear optimisation problem will be solved using an iterative routine that requires some initial starting guess for the current density. A standard minimum power current density solution is an appropriate choice of starting guess and also represents a good source of comparison for the minimum hot spot coils with regards to maximum temperature values and coil performance. Therefore the theory behind the design of minimum power gradient coils, similar to Forbes and Crozier [7], will be summarised briefly before details of the hot spot minimisation technique are elucidated.

We wish to obtain a current density solution $\mathbf{j}(\theta',z')$ (A/m) for the copper sheet displayed in Fig. 1, such that a linear magnetic field is induced within the spherical target region of radius c, centred at the origin, called the diameter spherical volume (DSV). Fourier series are used to describe the axial and azimuthal components of the current density, which must be divergence free, as well as the associated streamfunction (see also, [7]):

$$\psi(\theta',z') = \sum_{m=1}^{M}\sum_{n=1}^{N}\sin\left(\frac{n\pi(z'+L)}{2L}\right)[A_{mn}\cos m\theta' + B_{mn}\sin m\theta'], \tag{9}$$

$$j_\theta(\theta',z') = \sum_{m=1}^{M}\sum_{n=1}^{N}\frac{n\pi}{2L}\cos\left(\frac{n\pi(z'+L)}{2L}\right)[A_{mn}\cos m\theta' + B_{mn}\sin m\theta'], \tag{10}$$

$$j_z(\theta',z') = \sum_{m=1}^{M}\sum_{n=1}^{N}\frac{m}{a}\sin\left(\frac{n\pi(z'+L)}{2L}\right)[A_{mn}\sin m\theta' - B_{mn}\cos m\theta'], \tag{11}$$

where we have introduced the current density coefficients A_{mn} and $B_{mn} (m = 1 : M, n = 1 : N)$, which are to be solved for later. Contours of $\psi(\theta',z')$ provide appropriate coil winding locations for representing the current density in a discrete fashion.

Combining the Biot–Savart law (see for example, [18, p. 178]), Eqs. (10) and (11), and the change of variables $\beta = \theta' - \theta$, the following expression can be obtained for the axial component of the magnetic induction vector at the field point (r,θ,z):

$$B_z(r,\theta,z) = \mu_0\sum_{m=1}^{M}\sum_{n=1}^{N}U_{mn}(r,z)[A_{mn}\cos m\theta + B_{mn}\sin m\theta], \tag{12}$$

where

$$U_{mn}(r,z) = \frac{1}{2\pi}\int_{-L}^{L}\int_{0}^{\pi}\frac{n\pi}{2L}\frac{1}{R^3}a(a - r\cos\beta)\cos m\beta\cos\left(\frac{n\pi(z'+L)}{2L}\right)d\beta dz', \tag{13}$$

and

$$R = \left[a^2 + r^2 - 2ra\cos\beta + (z'-z)^2\right]^{1/2}. \tag{14}$$

The axial component (12) is of primary interest as it is this component in which the gradient field is defined.

Minimising the error between the induced field (12) and some target field on the surface of the DSV is an ill-posed problem and Tikhonov regularisation is used to obtain sensible current density solutions (see for example, [8, p. 307]). That is, a functional Γ, of the following form, is minimised with respect to the current density coefficients:

$$\Gamma = \Phi + \lambda_p\Pi. \tag{15}$$

The function Φ represents the field error between the axial component of the magnetic induction vector (12) and the desired target field on the surface of the DSV:

$$\Phi = c\int_{-c}^{c}\int_{-\pi}^{\pi}[B_z(r_T,\theta,z) - B_{Tz}(r_T,\theta,z)]^2 d\theta dz, \tag{16}$$

in which $r_T(z) = \sqrt{c^2 - z^2}$. The regularising parameter λ_P in Eq. (15) behaves in a similar way to a Lagrange multiplier except that its value is open for numerical experimentation. Lastly, the penalty function Π is a constraint that must be related quadratically to the current density and has been chosen in the present work to represent minimum power due to its intrinsic relationship to coil temperature:

$$\Pi = \int_{-L}^{L}\int_{-\pi}^{\pi}\mathbf{j}\cdot\mathbf{j}ad\theta' dz'. \tag{17}$$

Minimising the residual error, Γ (15), with respect to the unknown current density coefficients, results in a system of linear equations for these coefficients that can be expressed in the following matrix equation form:

$$(A + \lambda_P P)\mathbf{X} = \mathbf{T}. \tag{18}$$

Here matrix A (square) and vector $\mathbf{T}$ contain field error conditions resulting from Eq. (16) of the form:

$$\frac{\partial\Phi}{\partial A_{uv}} = 2\pi c\mu_0^2\sum_{n=1}^{N}A_{un}\int_{-c}^{c}U_{un}(r_T,z)U_{uv}(r_T,z)dz - 2c\mu_0\int_{-c}^{c}\int_{-\pi}^{\pi}B_{Tz}(r_T,\theta,z)U_{uv}(r_T,z)\cos u\theta d\theta dz. \tag{19}$$

Matrix P contains minimum power conditions resulting from Eq. (17) of the form:

$$\frac{\partial\Pi}{\partial A_{uv}} = 2\pi La\left[\left(\frac{v\pi}{2L}\right)^2 + \left(\frac{u}{a}\right)^2\right]A_{uv}. \tag{20}$$

The unknown current density coefficients are stored in vector $\mathbf{X}$ (of length $2MN$) and the solution to Eq. (18) can be used to calculate the current density using Eqs. (10) and (11), the magnetic field using Eq. (12), and the temperature distribution using Eq. (4). Discrete coil windings can be obtained by contouring the streamfunction ψ (9). Gradient homogeneity δ can be calculated using the expression of Turner [4] combined with a discrete form of the Biot–Savart law (field error $\sqrt{\delta}\times 100\%$). It is also straightforward to calculate other measures of coil performance such as efficiency η, by taking the ratio of the gradient field strength to the coil current magnitude, and inductance L (see for example, [9]). Note that it is common to quote some figure of merit that combines several properties of coil performance, such as $\eta^2/L(\mu T/A/m^4)$, which gives a measure that is independent of the number of windings [5].

2.3. Applying maximum temperature constraint

As indicated by Eq. (1), the temperature distribution depends heavily on the power in the coil, or $\mathbf{j}\cdot\mathbf{j}$. Therefore, designing a gradient coil by applying a minimum power constraint, as described above, results in a drop in the overall temperature of the coil. However, in the present paper we are interested in targeting specifically the spikes of high temperature in the distribution, or hot spots, rather than the average temperature. Indeed, to accommodate a drop in maximum temperature, the average temperature in the coil is free to rise such that the total energy of the coil remains sufficient to induce an adequately linear gradient field. Ideally, we would like to minimise a functional of the form of Eq. (15), in which the minimum power penalty function Π is replaced with some penalty function representing maximum coil temperature or some smoothing function of the temperature distribution such as $\|\nabla T\|^2$. However, a linear matrix Eq. (18) is only attainable if the penalty function Π is a quadratic function of current density, but this is not the case for the quantities $\max(T^*_{ssFS})$ and $\|\nabla T^*_{ssFS}\|^2$ considered here.

There are many techniques available for solving non-linear optimisation problems of this type (see for example, [19]). These methods typically require some initial starting guess at the solution and an iterative scheme is applied to obtain the optimum solution. The initial guess must be sufficiently close to the optimum solution and the iterative routine must be chosen carefully to guarantee convergence. For the present problem, a sensible starting guess for the current density solution is the minimum power solution of Eq. (15). For the iterative optimisation routine we consider a functional of the form:

$$\Omega = \Phi + \lambda_P\Pi + \lambda_Q\Lambda, \tag{21}$$

which is the same as Eq. (15) but with the extra term involving λ_Q and Λ. This functional Ω is minimised at each step of a fixed point iteration scheme in which λ_Q behaves in a similar way to the regularising parameter λ_P, and the second penalty function Λ relates to some feature of the coil that penalises the maximum temperature and is calculated using the current density solution from the previous iteration. For example, in the first iteration, the current density solution from solving Eq. (18) is used in the calculation of Λ in Eq. (21).

The best choice of the penalty function Λ for minimising the gradient hot spots is not obvious. For instance, using the $\max(T^*_{ssFS})$ value of the coil might seem reasonable; however, this retains no other information about the form of the temperature distribution or the current density and results in poor convergence. An alternative choice may be to use $\nabla^2 T^*_{ssFS}$ as a smoothing function; however, on inspection of the steady-state heat Eq. (3) it becomes apparent that this amounts to minimising the power and the average temperature, which does not reduce local hot spots. One choice of penalty function that has resulted in the greatest success with this work is to minimise the total square of the gradient of the temperature distribution, $\|\nabla T^*_{ssFS}\|^2$, over the coil. This effectively targets the slope at all points in the distribution and results in a smoothing and lowering of the hot spots. The penalty function can be calculated in a straightforward manner using the Fourier series form of Eq. (4). However, the complementary function type solution, T^*_{ssCF} (6), and particular integral type solution, T^*_{ssPI} (5), are considered separately such that difficult cross-terms are avoided in the derivation:

$$\Lambda = \Lambda_{PI} + \Lambda_{CF} = \int_{-L}^{3L}\int_{0}^{2\pi}\left\|\nabla T^*_{ssPI}\right\|^2 ad\theta' dz' + \int_{-L}^{L}\int_{0}^{2\pi}\left\|\nabla T^*_{ssCF}\right\|^2 ad\theta' dz'. \tag{22}$$

Note that the upper limit of the z'-integral for Λ_{PI} has been extended to $3L$ to take advantage of orthogonal properties in the expression for T^*_{ssPI} (5). Minimising the functional Ω (21) with respect to the current density coefficients demands the calculation of $\partial\Lambda_{PI}/\partial A_{uv}, \partial\Lambda_{PI}/\partial B_{uv}, \partial\Lambda_{CF}/\partial A_{uv}$ and $\partial\Lambda_{CF}/\partial B_{uv}$. Substituting Eq. (5) into the first term on the right hand side of Eq. (22) and differentiating with respect to the coefficient A_{uv} yields

$$\frac{\partial\Lambda_{PI}}{\partial A_{uv}} = 8a\pi L\sum_{m=1}^{M_T}\left(\frac{m}{a}\right)^2\left[F_{m0}\frac{\partial F_{m0}}{\partial A_{uv}} + G_{m0}\frac{\partial G_{m0}}{\partial A_{uv}}\right] + 8a\pi L\sum_{n=1}^{N_T}\left(\frac{n\pi}{2L}\right)^2\left[C_{0n}\frac{\partial C_{0n}}{\partial A_{uv}} + F_{0n}\frac{\partial F_{0n}}{\partial A_{uv}}\right] + 4a\pi L\sum_{m=1}^{M_T}\sum_{n=1}^{N_T}\left[\left(\frac{m}{a}\right)^2 + \left(\frac{n\pi}{2L}\right)^2\right]\left[C_{mn}\frac{\partial C_{mn}}{\partial A_{uv}} + D_{mn}\frac{\partial D_{mn}}{\partial A_{uv}} + F_{mn}\frac{\partial F_{mn}}{\partial A_{uv}} + G_{mn}\frac{\partial G_{mn}}{\partial A_{uv}}\right], \tag{23}$$

where, for example, C_{mn} is given by Eq. (7) and terms such as $\partial C_{mn}/\partial A_{uv}$ can be obtained from Eq. (7) and equivalent equations. A similar expression to Eq. (23) is obtained for $\partial\Lambda_{PI}/\partial B_{uv}$. The equivalent expressions involving Λ_{CF} in Eq. (22) are much more compli-

cated and have been left to an Appendix (see Eq. (25)). Note that for the results in the present paper, expressions such as Eq. (23) have been calculated exactly. The derivations are quite involved but lead to fast computation of results. Nevertheless it is possible to calculate, for example, $\partial\Lambda_{PI}/\partial A_{uv}$ and $\partial\Lambda_{CF}/\partial A_{uv}$ approximately using finite differences. This has also been tested and accurate solutions have been obtained requiring little explicit mathematical derivation, although at the expense of increased computer run-time.

As mentioned previously, the functional Ω, given in Eq. (21) must be minimised with respect to the Fourier coefficients at every iteration. This is accomplished using a two-step numerical scheme:

$$(1)\ \text{Solve}: \quad (A+\lambda_P P)\mathbf{X}_i = \mathbf{T} + \lambda_Q \mathbf{Q}(\mathbf{x}_i), \tag{24a}$$

$$(2)\ \text{Update}: \quad \mathbf{x}_{i+1} = \omega\mathbf{x}_i + (1-\omega)\mathbf{X}_i. \tag{24b}$$

Here, vector $\mathbf{x}_{i+1}$ contains updated current density coefficients and vector $\mathbf{x}_i$ contains current density coefficients from the previous iteration. That is, we solve a linear matrix Eq. (24a) at each iteration to minimise the functional Ω in Eq. (21). Iteration (24b) is necessary due to the non-linear constraint $\|\nabla T^*_{ssFS}\|^2$ in Eq. (22) and this adjusts the $2MN$ vector $\mathbf{x}$ of Fourier coefficients, A_{uv} and B_{uv}, at each step in the routine.

Eq. (24b) is in the form of a relaxed fixed point iteration routine, with relaxation parameter ω. Increasing ω improves the stability of convergence at the expense of a slower rate of convergence. The matrices A and P and the vector $\mathbf{T}$ in Eq. (24a) are the same as those in Eq. (18). The regularising parameter λ_P must be fixed at the value used to obtain the minimum power current density coefficients, which themselves are used as the initial guess $\mathbf{x}_0$ ($i=0$).

The vector $\mathbf{Q}$ in Eq. (24a) represents the function Λ (22) minimised with respect to the current density coefficients and hence contains terms such as those given by Eq. (23) and Eq. (25) in the Appendix. These terms are calculated using the current density coefficients obtained in the previous iteration $\mathbf{x}_i$. In addition, vector $\mathbf{Q}$ is multiplied by a symmetrising matrix at every step to ensure that a symmetric current density solution is retained. This sets to zero the elements of matrix $\mathbf{Q}$ that relate to odd n values of the current density (see Eqs. (10) and (11)) and is necessary to obtain a convergent solution with a lower maximum temperature.

Finally, the weighting λ_Q in Eq. (24a) controls the influence of the vector $\mathbf{Q}$ on the solution at each step. Increasing λ_Q results in a lower $\max(T^*_{ssFS})$ value; however, this also increases gradient homogeneity field error and if λ_Q is too large the iteration scheme may not converge. This problem can be countered to some extent by increasing the relaxation parameter ω in Eq. (24b) and hence a careful balance between the parameters ω and λ_Q must be investigated to achieve optimum results. Note that if $\lambda_Q = 0$ and $\omega = 0$ in Eq. (24), then this equation reduces to the minimum power matrix equation problem of Eq. (18). Therefore, increasing λ_Q in Eq. (24) adjusts the solution $\mathbf{x}$ from one that satisfies Eq. (18) to one that minimises $\|\nabla T^*_{ssFS}\|^2$, and introducing $\omega \neq 0$ limits the extent to which this solution $\mathbf{x}$ is adjusted at each iteration. Further discussion of ω and λ_Q values and methods to achieve convergence will be given in Section 3.

Once Eq. (24) has been iterated a sufficient number of times for adequate convergence, the solution $\mathbf{x}_{i+1}$ may be used to calculate several features of the gradient coil. These include the current density using Eqs. (10) and (11), the magnetic field using Eq. (12) and the temperature distribution using Eq. (4). Contouring the associated streamfunction (9) gives the coil winding pattern and also enables calculation of the field error $\sqrt{\delta}$, the coil efficiency η, and the inductance L for the discretised system, as described previously. It is important to compare the values $\max(T^*_{ssFS})$, $\sqrt{\delta}$, η and L for results obtained using the minimum hot spot temperature method of solving Eq. (24) to those obtained using the minimum power constraint alone by solving Eq. (18).

3. Results

In this section, results from implementing the iterative minimum hot spot temperature method, given by Eq. (24), will be displayed and discussed for a variety of cases. As described in Section 2, a minimum power current density solution to Eq. (18) will be required as a starting guess $\mathbf{x}_0$ for the numerical scheme in Eq. (24). In addition, the popularity of minimum power gradient coils demonstrates these to be a worthy source of comparison for the minimum hot spot designs to be presented later in this section. Therefore, a minimum power gradient coil will be presented firstly along with several corresponding temperature distributions assuming different thermal and cooling properties for the gradient system. These results will then be compared with subsequent results obtained using the minimum hot spot temperature method.

The chosen geometry for the cylindrical whole-body x-gradient coil, depicted in Fig. 1, consists of a copper sheet of radius $r_c = 0.25$ m, length $2L = 1$ m and width $w = 0.002$ m, embedded in an epoxy former of inner and outer thicknesses, $\Delta r_i = 0.002$ m and $\Delta r_o = 0.002$ m, respectively. The target field was chosen to be a 50 mT/m x-gradient field on the surface of a symmetrically located DSV of radius $c = 0.15$ m (see Fig. 1). The program MATLAB™ was used for all calculations, and the series representations in Eqs. (10) and (11) were taken to $M = N = 15$ terms and numerical integration was performed over 20 intervals.

Fig. 2 displays the winding pattern in the first quadrant of the minimum power gradient coil obtained by solving Eq. (18) with $\lambda_P = 10^{-18}$. This λ_P value reduced the condition number from the order 10^{23} to 10^4. The precise locations of the coil windings were obtained by contouring the streamfunction (9). For 52 coil windings carrying $I = 470$ A of current, the gradient homogeneity field error was found to be $\sqrt{\delta} = 0.69\%$, the efficiency 106 μT/A/m and the inductance 216 μH, such that $\eta^2/L = 52.5$ μT/A/m^4. These are typical coil performance values for an x-gradient coil of the dimensions described above.

Temperature distributions are plotted as coloured contour plots using Eq. (4), with numerical integration over 90 intervals and $M_T = N_T = 30$ terms, which takes 13 s to compute on a 2 GHz Intel Core2 CPU wiht 2 GB of RAM. Copper and epoxy material properties used in calculating Eq. (4) were given in Section 2. Fig. 3a displays the temperature distribution assuming forced air cooling at the inner and outer boundaries (i.e., $h_i = h_o = 100$ W/m^2/K). Hot spots are shown to occur near regions of high current density, or equivalently, where the coil windings are closely spaced.

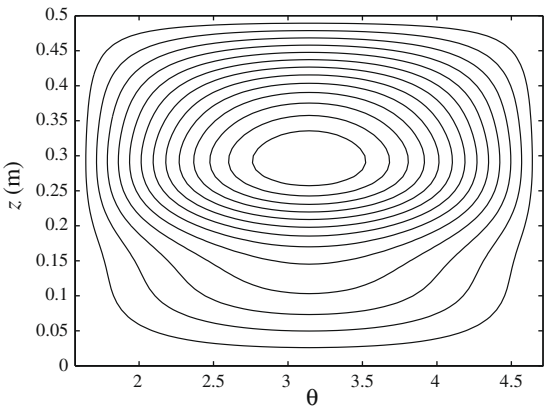

Fig. 2. The 13 coil windings for the first quadrant of the minimum power coil obtained by solving Eq. (18) with $\lambda_P = 10^{-18}$. Each winding carries 470 A of current such that the efficiency is 106 μT/A/m. The field error for a 0.15 m radius, symmetrically located DSV is $\sqrt{\delta} = 0.69\%$. The inductance is $L = 216$ μH such that the figure of merit is $\eta^2/L = 52.5$ μT/A/m^4.

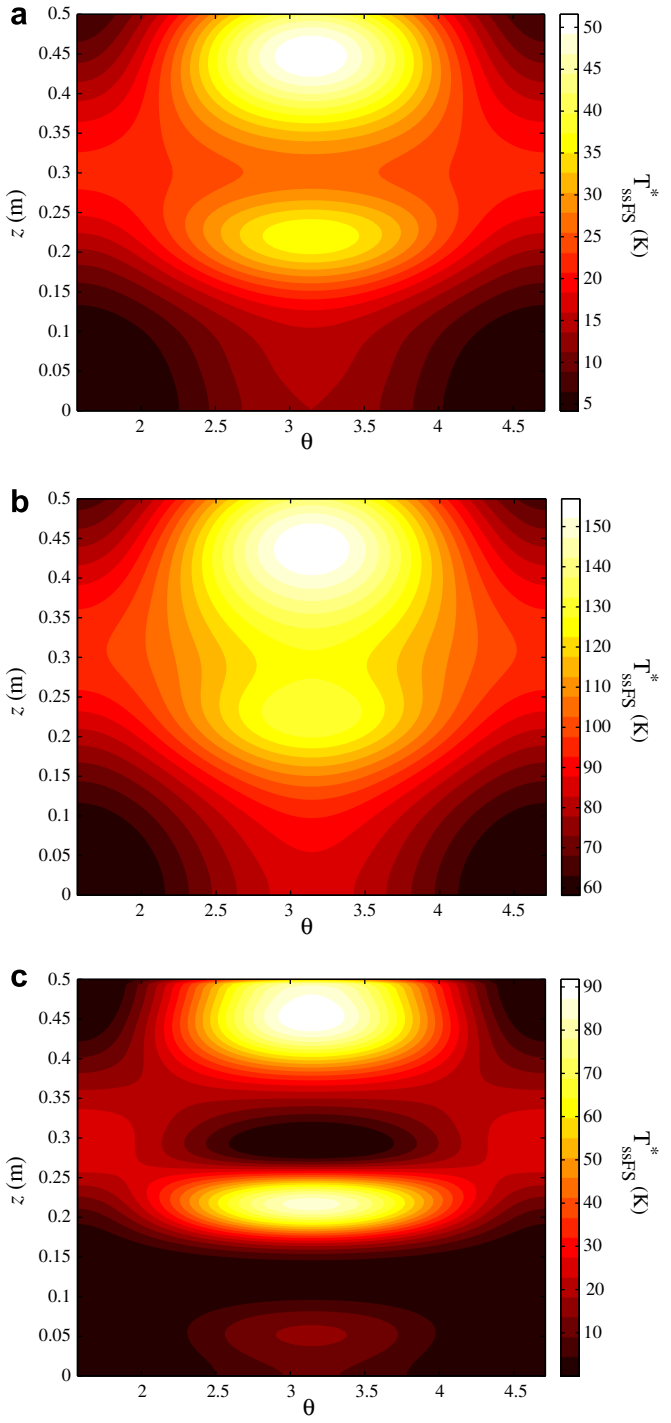

Fig. 3. The temperature distribution T^*_{ssFS} (4) for the gradient coil depicted in Fig. 2 assuming (a) a copper sheet ($k_c = 401$ W/m/K) and forced air cooling ($h_i = h_o = 100$ W/m^2/K), (b) a copper sheet ($k_c = 401$ W/m/K) and convective air cooling ($h_i = h_o = 10$ W/m^2/K), (c) heavily insulated coil windings ($k_c = 0.6$ W/m/K) and forced air cooling ($h_i = h_o = 100$ W/m^2/K).

The maximum hot spot temperature for this example is max $(T^*_{ssFS}) = 51.6$ K above ambient temperature. The hot spot temperature as a function of time can be obtained by solving Eq. (1) approximately as described in Section 2. For this forced air cooled case the time taken to reach 95% maximum temperature is 71.3 s, which demonstrates that the steady-state solution of Fig. 3a will occur over the course of a typical scanning scenario. This result matches well with the model of Chu and Rutt [13], which was verified experimentally.

Fig. 3b shows the result when the level of cooling is reduced to that of convective air alone (i.e., $h_i = h_o = 10$ W/m^2/K). This leads to a higher hot spot temperature of max $(T^*_{ssFS}) = 156.9$ K above ambient temperature and an elevated overall temperature that is much more evenly spread out across the copper layer, as expected with the lower level of cooling due to less heat being removed radially. The temperature rise-time is approximately three times longer for the convective air cooled coil; nevertheless, these hot spot values demonstrate the importance of adequate cooling within the coil system. Note that for forced water cooling (i.e., $h_i = h_o = 1000$ W/m^2/K) the hot spot temperature is reduced greatly to 22.9 K above ambient temperature.

A third example is shown in Fig. 3c for a forced air cooled coil (i.e., $h_i = h_o = 100$ W/m^2/K) but with different assumed thermal properties for the copper layer. That is, in many coils it is normal to cut distinct copper wires and fix them with epoxy resin within the former, rather than have a single complete copper sheet. This regime will lead to a much higher level of insulation and an upper bound for this effect is to set the thermal conductivity of the copper equal to that of the epoxy, ie $k_c = 0.6$ W/m/K. As shown in Fig. 3c, this results in much more distinct hot spots, as a result of the slower axial and azimuthal transfer of heat in this heavily insulated case, and an elevated maximum temperature of max $(T^*_{ssFS}) = 91.8$ K. In reality, the temperature distribution for a forced air cooled coil is likely to lie somewhere between that shown in Fig. 3a and that shown in Fig. 3c.

With the aim of reducing the hot spot temperature, an x-gradient coil was designed by solving the relaxed fixed point iteration scheme described by Eq. (24). The minimum power solution, depicted in Fig. 2, is used as a starting guess $\mathbf{x}_0$ for evaluating vector $\mathbf{Q}$ in Eq. (24a). This requires the calculation of terms such as those in Eqs. (23) and (25) in the Appendix, or alternatively $\mathbf{Q}$ can be obtained approximately using a finite differencing scheme as described in Section 2. The $\mathbf{Q}$ vector is symmetrised by setting to zero elements corresponding to odd n terms of the current density components, given in Eqs. (10) and (11), such that sensible coil winding solutions are retained and the hot spot temperature decreases.

Care must be taken in selecting the weighting λ_Q and the relaxation parameter ω in Eq. (24), and the non-linear optimisation routine must be iterated and tested for convergence. A great number of combinations of λ_Q and ω values were trialled. As mentioned in Section 2, increasing λ_Q results in a greater decrease in max (T^*_{ssFS}); however, if λ_Q is too large the routine will not converge. It is possible to overcome this problem in some cases by increasing the value of the relaxation parameter ω, which improves the stability of convergence. However, this also results in a slower rate of convergence and tends to elevate the final max (T^*_{ssFS}) value. In addition, these values also affect the field error $\sqrt{\delta}$, efficiency η and inductance L and so a careful selection of λ_Q and ω must be made.

Note that an alternative means of considering a high λ_Q value is to use a process called parameter homotopy. This involves a multi-step routine whereby Eq. (24) is iterated several times using a low λ_Q value to obtain a convergent solution for $\mathbf{x}$. This solution is then used as the initial guess in Eq. (24) using a higher λ_Q value and the process is repeated until the desired λ_Q is reached. This technique is successful in improving convergence as the solution $\mathbf{x}$ is adjusted by only a small amount with each successive increase in λ_Q.

Nevertheless, for the results presented in this paper, convergence was achieved by selecting a suitable ω value for a given λ_Q value and fixing these parameters when iterating Eq. (24). This typically required ω to be in the range $0.6 < \omega < 0.95$ and λ_Q to be of the order $10^{-14} - 10^{-16}$ and negative. Alternatively, an over-relaxed regime could be considered in which, for example, $\omega = 1.2$ or $\omega = 1.4$ (i.e., $\omega > 1$). For these cases, λ_Q must be positive for Eq. (24) to converge; however, over-relaxed fixed point iteration was found to be highly sensitive to ω and λ_Q values and superior convergence and results were obtained for $\omega < 1$ and negative λ_Q.

Table 1
Convergence of minimum hot spot temperature method, Eq. (24), for copper sheet ($k_c = 401$ W/m/K) with forced air cooling ($h_i = h_o = 100$ W/m^2/K) and the optimisation parameters $\lambda_Q = -5 \times 10^{-15}$ and $\omega = 0.8$.

	Max(T^*_{ssFS}) (K)	Norm$(\mathbf{x}_{i+1} - \mathbf{x}_i)$
$\mathbf{x}_0$	51.6	–
$\mathbf{x}_1$	44.7	3.1×10^2
$\mathbf{x}_2$	41.3	7.5×10^1
$\mathbf{x}_3$	40.6	3.9×10^1
$\mathbf{x}_4$	40.1	2.2×10^1
$\mathbf{x}_5$	39.8	1.5×10^1
$\mathbf{x}_6$	39.6	1.0×10^1
$\mathbf{x}_7$	39.5	7.2×10^0
$\mathbf{x}_8$	39.4	5.2×10^0

Table 1 demonstrates the drop in max(T^*_{ssFS}) value over 8 iterations of Eq. (24) with $\lambda_Q = -5 \times 10^{-15}$ and $\omega = 0.8$, for a copper sheet gradient coil ($k_c = 401$ W/m/K) with forced air cooling ($h_i = h_o = 100$ W/m^2/K). We observe a 13.3% drop in the hot spot temperature relative to the environment in the first iteration alone and in total a 23.6% drop after 8 iterations to give max $(T^*_{ssFS}) = 39.4$ K. The column norm$(\mathbf{x}_{i+1} - \mathbf{x}_i)$ of Table 1 demonstrates the convergence of the current density solution for this example.

Fig. 4 shows the coil windings in one quadrant of the coil for the current density solution obtained after 8 iterations of Eq. (24) with the parameters described above. Comparing Fig. 4 to that for the minimum power coil of Fig. 2, we note a spreading of the windings in the denser regions of the coil and a squaring off of coil windings in other regions to accommodate this redistribution. The corresponding temperature distribution is shown in Fig. 5 which displays a much greater spreading of the hot spots, at the lower maximum temperature of max $(T^*_{ssFS}) = 39.4$ K above ambient, when compared to Fig. 3a for the minimum power coil.

The results shown in Fig. 5 demonstrate a very considerable improvement in hot spot temperature. However, this improvement does come at the cost of an increase in field error $\sqrt{\delta} = 0.86\%$ and inductance $L = 220$ μH. Nevertheless the windings require a lower coil current $I = 455$ A, leading to an improved efficiency of $\eta = 110$ μT/A/m and hence a higher coil performance figure of merit $\eta^2/L = 55.0$ μT/A/m^4, when compared to the minimum power coil of Fig. 2. Results for this minimum hot spot temperature solution, and those for subsequent examples, have been summarised in Table 2.

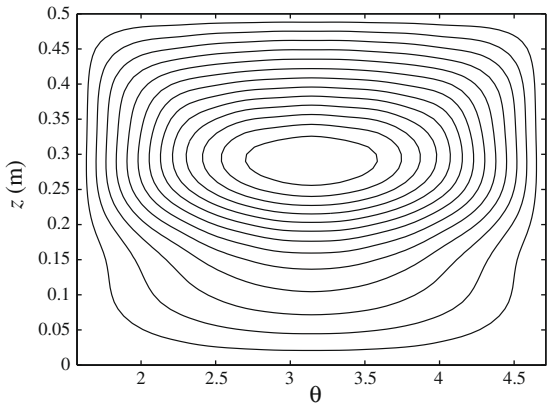

Fig. 4. The 13 coil windings obtained in the first quadrant of the minimum hot spot temperature coil after 8 iterations of Eq. (24) with $\lambda_Q = -5 \times 10^{-15}, \omega = 0.8$, and setting $k_c = 401$ W/m/K and $h_i = h_o = 100$ W/m^2/K (forced air cooling) in constructing vector **Q**. Each winding carries 455 A of current such that the efficiency is 110 μT/A/m. The field error for a 0.15 m radius, symmetrically located DSV is $\sqrt{\delta} = 0.86\%$. The inductance is $L = 220$ μH such that the figure of merit is $\eta^2/L = 55.0$ μT/A/m^4.

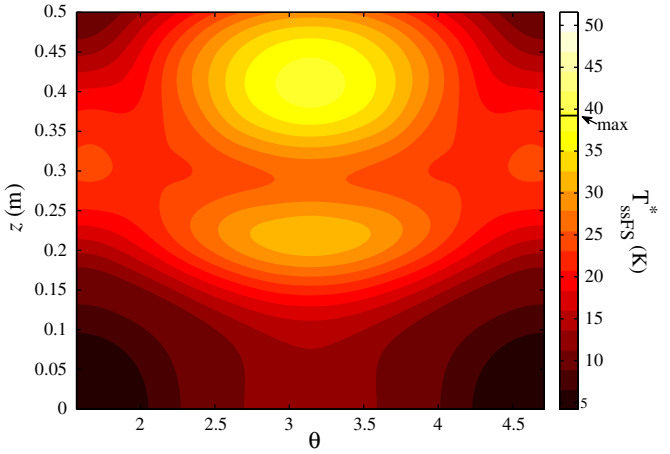

Fig. 5. The temperature distribution T^*_{ssFS} (4) for the gradient coil depicted in Fig. 4 assuming a copper sheet ($k_c = 401$ W/m/K) and forced air cooling ($h_i = h_o = 100$ W/m^2/K). Comparing to Fig. 3a we note that the hot spots are more spread out and at a lower maximum of max $(T^*_{ssFS}) = 39.4$ K above ambient temperature.

It is important to compare the drop in maximum temperature obtained through the use of Eq. (24), and the corresponding current density solution, with that obtained by increasing λ_P in the minimum power linear optimisation problem of Eq. (18). For a regularising parameter approximately equal to $\lambda_P = 3.7 \times 10^{-18}$, we get a current density solution with the same maximum temperature as the minimum hot spot solution, that is max $(T^*_{ssFS}) = 39.4$ K. However, the corresponding field error is much greater at $\sqrt{\delta} = 1.21\%$, compared to $\sqrt{\delta} = 0.86\%$ for the minimum hot spot coil. The coil performance, on the other hand, is found to be superior for the minimum power result with a figure of merit $\eta^2/L = 59.5$ μT/A/m^4. Nevertheless, this increase in coil performance is most likely associated with the increase in field error. Therefore an alternative comparison must be made involving the field error of solutions obtained using the two optimisation methods.

For a regularising parameter approximately equal to $\lambda_P = 1.7 \times 10^{-18}$, we get a current density solution from Eq. (18) with the same field error as the minimum hot spot solution of Fig. 4, that is $\sqrt{\delta} = 0.86\%$. This is also found to have the same coil performance figure of merit $\eta^2/L = 55.0$ μT/A/m^4. However, whereas the minimum hot spot method yields a gradient coil with a maximum temperature of max$(T^*_{ssFS}) = 39.4$ K, the minimum power method yields a coil with max$(T^*_{ssFS}) = 46.8$ K (see Table 2). That is, for an equivalent field error and coil performance, use

Table 2
Example results for hot spot temperature minimisation for different thermal and cooling properties. Results for equivalent minimum power cases (by field error) are given in square parentheses.

	Case 1	Case 2	Case 3[a]
k_c (W/m/K)	401	401	0.6
$h_i = h_o$ (W/m^2/K)	100	10	100
λ_Q	-5×10^{-15}	-2×10^{-15}	-5×10^{-15}
ω	0.8	0.8	0.8
Max(T^*_{ssFS}) (K)	39.4 [46.8]	122.8 [136.6]	64.6 [81.6]
$\sqrt{\delta}$ (%)	0.86 [0.86]	0.97 [0.97]	0.86 [0.86]
I (A)	455	437	455
η (μT/A/m)	110	114	110
L (μH)	220	230	220
η^2/L (μT/A/m^4)	55.0 [55.0]	57.0 [56.6]	55.0 [55.0]

[a] Case 3 temperature results have been calculated using the current density from Case 1, rather than recalculating vector **Q**.

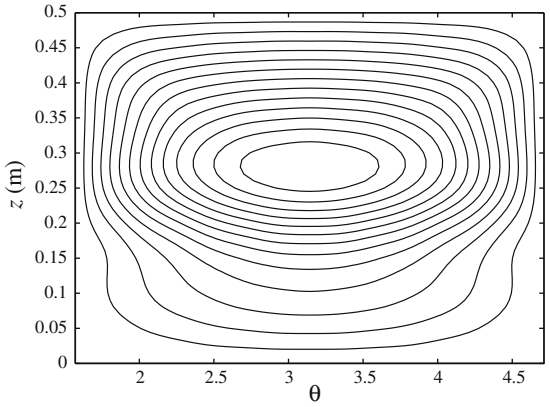

Fig. 6. The 13 coil windings obtained in the first quadrant of the minimum hot spot temperature coil after 8 iterations of Eq. (24) with $\lambda_Q = -2 \times 10^{-15}, \omega = 0.8$, and setting $k_c = 401$ W/m/K and $h_i = h_o = 10$ W/m^2/K (convective air cooling) in constructing vector **Q**. Each winding carries 437 A of current such that the efficiency is 114 μT/A/m. The field error for a 0.15 m radius, symmetrically located DSV is $\sqrt{\delta} = 0.97\%$. The inductance is $L = 230$ μH such that the figure of merit is $\eta^2/L = 57.0$ μT/A/m^4.

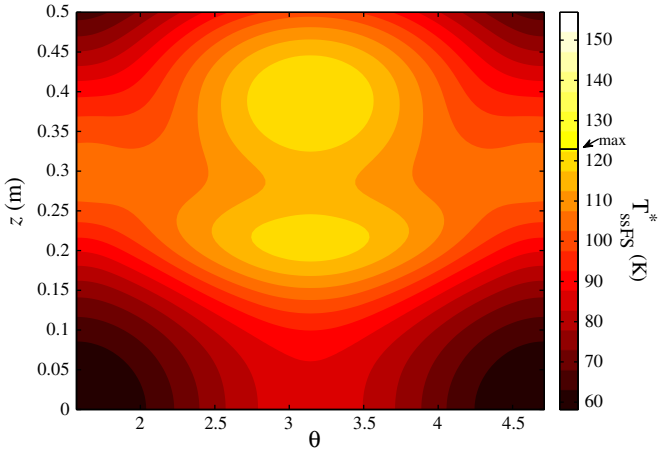

Fig. 7. The temperature distribution T^*_{ssFS} (4) for the gradient coil depicted in Fig. 6 assuming a copper sheet ($k_c = 401$ W/m/K) and convective air cooling ($h_i = h_o = 10$ W/m^2/K). Comparing to Fig. 3b we note that the hot spots are more spread out and at a lower maximum of max $(T^*_{ssFS}) = 122.8$ K above ambient temperature.

of the minimum hot spot method (24), for this example, results in a maximum temperature relative to the environment that is 15.8% lower than that obtained by using the minimum power method (18).

We can use Eq. (24) to design a coil with reduced hot spot temperature for the case of convective air cooling by setting $h_i = h_o = 10$ W/m^2/K when evaluating vector **Q**. Of course, it is possible to evaluate the temperature distribution for the coil windings in Fig. 4 assuming convective air cooling rather than forced air cooling and a drop in hot spot temperature will be observed. Nevertheless, modifying vector **Q** and repeating the iterations yields a superior result for this case. Fig. 6 displays the coil winding solution after 8 iterations with $\lambda_Q = -2 \times 10^{-15}$ and $\omega = 0.8$, which is clearly similar to that shown in Fig. 4. That is, there are less dense regions of current density and a slight squaring off of coil windings when compared to the original minimum power result of Fig. 2. The corresponding temperature distribution is shown in Fig. 7 in which we again observe considerable spreading out of the hot spot over a greater area of the coil at a much lower temperature $(\max(T^*_{ssFS}) = 122.8$ K), when compared to the original temperature distribution for convective air cooling of Fig. 3b $(\max(T^*_{ssFS}) = 156.9$ K).

For the convective air cooling result of Fig. 6 the hot spot temperature is 122.8 K above ambient, the field error is 0.97% and the coil performance figure of merit is 57.0 μT/A/m^4 (see Table 2). A minimum power current density with the same field error can be obtained by solving Eq. (18) with $\lambda_P = 2.2 \times 10^{-18}$. This minimum power result is actually found to have a slightly inferior coil performance of 56.6 μT/A/m^4 and a much higher maximum temperature value of 136.6 K. This is a very considerable result and demonstrates the great utility of the minimum hot spot temperature optimisation method of Eq. (24).

As a final example we may again consider the more heavily insulated case of setting $k_c = 0.6$ W/m/K. For this example, recalculating **Q** and iterating Eq. (24) leads to an inferior result to just computing the temperature distribution for the coil windings in Fig. 4 with $k_c = 0.6$ W/m/K instead of $k_c = 401$ W/m/K. This is likely due to the term $h_t/k_c w$ in Eqs. (23) and (25) becoming too large and swamping those terms depending on the current density modes m and n, which subsequently hampers the optimisation routine. Fig. 8 displays the temperature distribution for the coil windings in Fig. 4 but with $k_c = 0.6$ W/m/K and shows a considerable smearing of the hot spot near the coil end, with a lower maximum temperature, when compared to Fig. 3c for the original coil of Fig. 2. The maximum temperature value for this example is found to be greatly reduced to 64.6 K above ambient temperature (29.6% improvement), whereas the equivalent minimum power coil has a maximum temperature of 81.6 K. That is, the minimum hot spot result for this heavily insulated case has a maximum temperature value that is 20.9% less than that of a minimum power coil with the same $\sqrt{\delta}$ and η^2/L values. This represents a vast improvement in hot spot temperature at no cost to coil performance. Note that for the true case of discrete coil windings embedded in the coil former, it is reasonable to expect a result that lies somewhere between the copper sheet case depicted in Fig. 5 and the heavily insulated case in Fig. 8.

4. Conclusion

A model has been presented for calculating the spatial temperature distribution of gradient coils and then redesigning these coils to have improved temperature distributions and lower hot spot temperatures when compared to standard minimum power designs. The temperature distribution model includes Ohmic heating

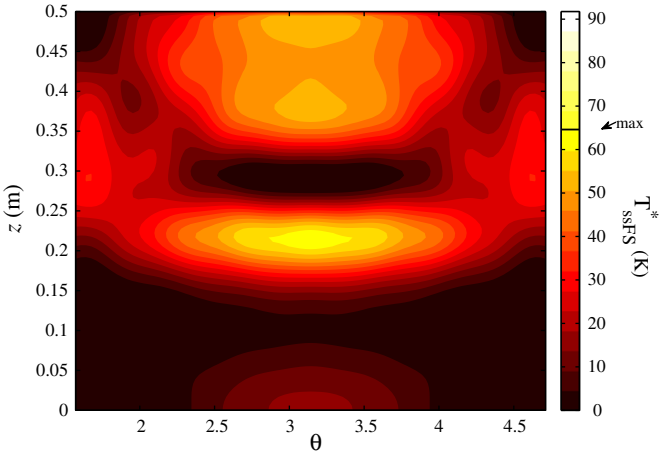

Fig. 8. The temperature distribution T^*_{ssFS} (4) for the gradient coil depicted in Fig. 4 assuming heavily insulated coil windings ($k_c = 0.6$ W/m/K) and forced air cooling ($h_i = h_o = 100$ W/m^2/K). Comparing to Fig. 3c we note that the hot spots are considerably more spread out and at a lower maximum of max $(T^*_{ssFS}) = 64.6$ K above ambient temperature.

by a current density, conduction through a copper layer and insulating former, and convection and radiation to a cooled environment. Maximum temperature corresponds to a non-linear constraint and this was represented by the total square of the gradient of the temperature over the coil and minimised using a relaxed fixed point iteration scheme. Minimum power coil windings were used as an initial guess in the optimisation routine and were altered with each iteration yielding a winding pattern with greater coil spacing, a more spread out temperature distribution and lower maximum temperature.

The method was applied to the design of a number of gradient coils assuming different cooling mechanisms and thermal properties within the coil system. For all examples considered, coil winding solutions were obtained that displayed considerably lower hot spot temperatures when compared to standard minimum power gradient coils with equivalent gradient homogeneity field error and coil performance parameters of efficiency and inductance. That is, maximum coil temperature was reduced, in some cases by over 20% relative to ambient temperature, at no cost to field error or coil performance using the optimisation method presented in this paper.

The non-linear temperature constraint can be calculated exactly with some derivation or approximately using a simple finite differencing scheme. The optimisation method is semi-analytic in nature, straightforward to construct and takes the order of minutes to run on a standard desktop computer. In addition, non-linear constraints other than maximum temperature may be included easily in the optimisation routine presented in this paper, and the method is adaptable to other coil geometries.

The combined temperature distribution model and hot spot minimisation method provide a great utility in examining the temperature profile of gradient coils prior to construction and offering a means of adjusting the locations of coil windings to reduce hot spot temperature considerably. In future work, the model may be applied to asymmetric gradient coils which contain troublesome dense regions of coil windings and higher hot spot temperatures. In addition, an optimisation method may be devised for the precise location of cooling pipes within the gradient system.

Appendix A

Minimising Eq. (22) with respect to the current density coefficients, demands calculation of $\partial\Lambda_{CF}/\partial A_{uv}$ and $\partial\Lambda_{CF}/\partial B_{uv}$. Substituting Eq. (6) into the second term on the right-hand side of Eq. (22) and differentiating with respect to the coefficient A_{uv} yields:

$$\begin{aligned}\frac{\partial\Lambda_{CF}}{\partial A_{uv}} = {} & 2a\pi\sqrt{\frac{h_t}{k_c w}}\left[\exp\left(2\sqrt{\frac{h_t}{k_c w}}L\right)-\exp\left(-2\sqrt{\frac{h_t}{k_c w}}L\right)\right]\\ & \times\sum_{n=0}^{N_T}\left[J_0\frac{\partial J_0}{\partial F_{0n}}\frac{\partial F_{0n}}{\partial A_{uv}}+P_0\frac{\partial P_0}{\partial F_{0n}}\frac{\partial F_{0n}}{\partial A_{uv}}\right]-8a\pi L\left(\frac{h_t}{k_c w}\right)\\ & \times\sum_{n=0}^{N_T}\left[P_0\frac{\partial J_0}{\partial F_{0n}}\frac{\partial F_{0n}}{\partial A_{uv}}+J_0\frac{\partial P_0}{\partial F_{0n}}\frac{\partial F_{0n}}{\partial A_{uv}}\right]+a\pi\sum_{m=1}^{M_T}\sum_{n=0}^{N_T}\frac{\left(2\left(\frac{m}{a}\right)^2+\frac{h_t}{k_c w}\right)}{\sqrt{\left(\frac{m}{a}\right)^2+\frac{h_t}{k_c w}}}\\ & \times\left[\exp\left(2\sqrt{\left(\frac{m}{a}\right)^2+\frac{h_t}{k_c w}}L\right)-\exp\left(-2\sqrt{\left(\frac{m}{a}\right)^2+\frac{h_t}{k_c w}}L\right)\right]\\ & \times\left[J_m\frac{\partial J_m}{\partial F_{mn}}\frac{\partial F_{mn}}{\partial A_{uv}}+K_m\frac{\partial K_m}{\partial G_{mn}}\frac{\partial G_{mn}}{\partial A_{uv}}+P_m\frac{\partial P_m}{\partial F_{mn}}\frac{\partial F_{mn}}{\partial A_{uv}}\right.\\ & \left.+Q_m\frac{\partial Q_m}{\partial G_{mn}}\frac{\partial G_{mn}}{\partial A_{uv}}\right]-4a\pi L\left(\frac{h_t}{k_c w}\right)\sum_{m=1}^{M_T}\sum_{n=0}^{N_T}\left[P_m\frac{\partial J_m}{\partial F_{mn}}\frac{\partial F_{mn}}{\partial A_{uv}}\right.\\ & \left.+Q_m\frac{\partial K_m}{\partial G_{mn}}\frac{\partial G_{mn}}{\partial A_{uv}}+J_m\frac{\partial P_m}{\partial F_{mn}}\frac{\partial F_{mn}}{\partial A_{uv}}+K_m\frac{\partial Q_m}{\partial G_{mn}}\frac{\partial G_{mn}}{\partial A_{uv}}\right],\end{aligned}\tag{25}$$

where, for example, P_m is given by Eq. (8), terms such as $\partial P_m/\partial F_{mn}$ can be obtained from Eq. (8) and equivalent equations, and terms such as $\partial F_{mn}/\partial A_{uv}$ can be obtained from equations similar to Eq. (7). A similar expression to Eq. (25) is obtained for $\partial\Lambda_{CF}/\partial B_{uv}$. Note that, as mentioned in Section 2, it is possible to obtain $\partial\Lambda_{CF}/\partial A_{uv}$ and $\partial\Lambda_{CF}/\partial B_{uv}$ approximately using finite differencing at the expense of extended computer run-time.

References

[1] R. Turner, A target field approach to optimal coil design, J. Phys. D Appl. Phys. 19 (8) (1986) L147–L151.
[2] R. Turner, Minimum inductance coils, J. Phys. E Sci. Instrum. 21 (10) (1988) 948–952.
[3] D.I. Hoult, R. Deslauriers, Accurate shim-coil design and magnet-field profiling by a power-minimization-matrix method, J. Magn. Reson. Ser. A 108 (1) (1994) 9–20.
[4] R. Turner, Gradient coil design — a review of methods, Magn. Reson. Imaging 11 (7) (1993) 903–920.
[5] J.W. Carlson, K.A. Derby, K.C. Hawryszko, M. Weideman, Design and evaluation of shielded gradient coils, Magn. Reson. Med. 26 (2) (1992) 191–206.
[6] B.A. Chronik, B.K. Rutt, Constrained length minimum inductance gradient coil design, Magn. Reson. Med. 39 (2) (1998) 270–278.
[7] L.K. Forbes, S. Crozier, A novel target-field method for magnetic resonance shim coils: III. Shielded zonal and tesseral coils, J. Phys. D Appl. Phys. 36 (2) (2003) 68–80.
[8] L.M. Delves, J.L. Mohamed, Computational Methods for Integral Equations, Cambridge University Press, Cambridge, UK, 1985.
[9] P.T. While, L.K. Forbes, S. Crozier, 3-D gradient coil design-initial theoretical framework, IEEE Trans. Biomed. Eng. 56 (4) (2009) 1169–1183, doi:10.1109/TBME.2009.2013199.
[10] C.F. Maier, H.N. Nikolov, K.C. Chu, B.A. Chronik, B.K. Rutt, Practical design of a high-strength breast gradient coil, Magn. Reson. Med. 39 (3) (1998) 392–401.
[11] B.A. Chronik, A. Alejski, B.K. Rutt, Design and fabrication of a three-axis edge ROU head and neck gradient coil, Magn. Reson. Med. 44 (6) (2000) 955–963.
[12] B. Aksel, L. Marinelli, B.D. Collick, C. Von Morze, P.A. Bottomley, C.J. Hardy, Local planar gradients with order-of-magnitude strength and speed advantage, Magn. Reson. Med. 58 (1) (2007) 134–143, doi:10.1002/mrm.21263.
[13] K.C. Chu, B.K. Rutt, MR gradient coil heat dissipation, Magn. Reson. Med. 34 (1) (1995) 125–132.
[14] M. Poole, H.S. Lopez, S. Crozier, Adaptively regularized gradient coils for reduced local heating, Concepts Magn. Reson. B Magn. Reson. Eng. 33B (4) (2008) 220–227, doi:10.1002/cmr.b.20125.
[15] J. Leggett, S. Crozier, R.W. Bowtell, Actively shielded multi-layer gradient coil designs with improved cooling properties, J. Magn. Reson. 165 (2) (2003) 196–207, doi:10.1016/j.jmr.2003.08.002.
[16] A.J. Chapman, Heat Transfer, fourth ed., Macmillan Publishing Company, New York, 1984.
[17] L.C. Thomas, Fundamentals of Heat Transfer, Prentice-Hall Inc., Englewood Cliffs, NJ, 1980.
[18] J.D. Jackson, Classical Electrodynamics, third ed., John Wiley & Sons Inc., New York, 1999.
[19] D.A. Wismer, R. Chattergy, Introduction to Nonlinear Optimization, Elsevier North-Holland Inc., New York, 1978.